TO APPEAR IN THE ASTROPHYSICAL JOURNAL
Preprint typeset using LaTeX style emulateapj v. 04/03/99

arXiv:astro-ph/9909391v1 23 Sep 1999

DETECTION AND PHOTOMETRY OF HOT HORIZONTAL BRANCH STARS IN THE CORE OF M32[1]

THOMAS M. BROWN[2], CHARLES W. BOWERS, RANDY A. KIMBLE, ALLEN V. SWEIGART
Laboratory for Astronomy & Solar Physics, Code 681, NASA/GSFC, Greenbelt, MD 20771. tbrown@pulsar.gsfc.nasa.gov, bowers@band2.gsfc.nasa.gov, kimble@ccd.gsfc.nasa.gov, sweigart@bach.gsfc.nasa.gov.

HENRY C. FERGUSON
Space Telescope Science Institute, 3700 San Martin Drive, Baltimore, MD 21218. ferguson@stsci.edu.

To appear in The Astrophysical Journal

ABSTRACT

We present the deepest near-UV image of M32 to date, which for the first time resolves hot horizontal branch (HB) stars in an elliptical galaxy. Given the near-solar metallicity of M32, much larger than that of globular clusters, the existence of an extended horizontal branch is a striking example of the second parameter effect, and, most importantly, provides direct evidence that hot HB stars and their progeny are the major contributors to the UV upturn phenomenon observed in elliptical galaxies. Our image, obtained with the Space Telescope Imaging Spectrograph (STIS), detects approximately 8000 stars in a $25'' \times 25''$ field, centered $7.7''$ from the galaxy nucleus. These stars span a range of 21–28 mag in the STMAG system, and in the deepest parts of the image, our catalog is reasonably complete ($> 25\%$) to a magnitude of 27. The hot HB spans a magnitude range of 25–27 mag at effective temperatures hotter than 8500 K. We interpret this near-UV luminosity function with an extensive set of HB and post-HB evolutionary tracks.

Although the UV-to-optical flux ratio in M32 is weak enough to be explained solely by the presence of post-asymptotic giant branch (post-AGB) stars, our image conclusively demonstrates that it arises from a small fraction ($\lesssim$5%) of the population passing through the hot HB phase. The production of these hot HB stars does not appear to rely upon dynamical mechanisms – mechanisms that may play a role in the HB morphology of globular clusters. The majority of the population presumably evolves through the red HB and subsequent post-AGB phases; however, we see far fewer UV-bright stars than expected from the lifetimes of canonical hydrogen-burning low-mass post-AGB tracks. There are several possible explanations: (1) the transition from AGB to $T_{\rm eff} > 60000$ K could be much more rapid than previously thought; (2) the vast majority of the post-AGB stars could be evolving along helium-burning tracks; (3) the post-AGB stars could be surrounded by circumstellar dust during the transition from the AGB to $T_{\rm eff} > 60000$ K.

Subject headings: galaxies: evolution — galaxies: abundances — galaxies: stellar content — ultraviolet: galaxies — ultraviolet: stars — stars: evolution

1. INTRODUCTION

The nearest elliptical galaxy available for study is M32, a companion to M31. Because M32 has a high surface brightness that is centrally concentrated, a near-solar metallicity, and a predominantly old population, it is usually considered a "compact elliptical" galaxy, as opposed to a "dwarf elliptical" or "dwarf spheroidal" (see Da Costa 1997). Due to its proximity (770 kpc), space-based observations are able to resolve individual cool stars near its center. Hot stars can also be detected in the center itself, because they are relatively rare, so crowding is not serious, and because the cooler, dominant populations are suppressed in the solar-blind UV bandpasses. Because M32 can be studied through colors, spectra, luminosity functions, and color-magnitude diagrams, it represents a natural benchmark in our understanding of elliptical galaxies.

Stellar population studies of M32 at optical and infrared wavelengths have shown no evidence for an extended horizontal branch (HB) (Grillmair et al. 1996), and population synthesis work often assumes that the galaxy has a "red clump" HB morphology (e.g., Worthey 1994). In the ultraviolet, Brown et al. (1998) found indirect evidence for an extended HB in M32: the UV-bright post-HB stars apparently follow evolutionary tracks originating from the hot end of the HB. In spectral synthesis studies, the assumption of a red clump HB morphology contributes to the need for an intermediate-age component to the stellar population, to provide the necessary ultraviolet flux (see Grillmair et al. 1996 and references therein). Direct proof of an extended HB would therefore relax the requirement that M32 has a composite population, with a dominant old component (of age 8 Gyr or more), and a minority younger component (of age $\sim$5 Gyr).

Considered as an extreme case in the sequence of true elliptical galaxies, M32 has the weakest UV-to-optical flux ratio measured to date ($1550 - V = 4.5$ mag; Burstein et al. 1988). Known as the UV upturn, the sharp rise in the spectra of elliptical galaxies at wavelengths shorter than 2500 Å was discovered with the OAO-2 satellite (Code 1969). Prior to this discovery, researchers did not expect such a UV-bright component in supposedly old, passively-evolving populations. Many candidates were suggested to explain the upturn, including young massive stars, hot white dwarfs, hot HB and post-HB stars, and non-thermal activity (for a complete review, see Greggio & Renzini 1990; O'Connell 1999). As the measurements of lo-

[1]Based on observations with the NASA/ESA Hubble Space Telescope obtained at the Space Telescope Science Institute, which is operated by the Association of Universities for Research in Astronomy, Incorporated, under NASA contract NAS 5-26555.

[2] NOAO Research Associate.

cal ellipticals were expanded, IUE observations demonstrated a large variation in the strength of the UV upturn from galaxy to galaxy, even though the spectra of ellipticals appear very similar at longer wavelengths. Characterized by the $1550-V$ color, the UV upturn becomes stronger and bluer as the metallicity (optical Mg_2 index) of the galaxy increases, while visible colors become redder (Burstein et al. 1988).

Today, it is widely believed that HB stars and their progeny are responsible for the far-UV emission in elliptical galaxies. There are three classes of post-HB evolution, each evolving from a different range of effective temperature on the zero-age HB (ZAHB; see Figure 1). Following core helium exhaustion, stars on the red end of the HB will evolve up the asymptotic giant branch (AGB), undergo thermal pulses, evolve as bright post-AGB stars to hotter temperatures, possibly form planetary nebulae, and eventually descend the white dwarf (WD) cooling curve. At hotter temperatures (and lower envelope masses) on the HB, stars will follow post-early AGB evolution: they evolve up the AGB, but leave the AGB before the thermal pulsing phase, continue to high temperatures at high luminosity, and descend the WD cooling curve. The bluest HB stars, with very little envelope mass, will follow AGB-Manqué evolution, evolving directly to hotter temperatures and brighter luminosities without ever ascending the AGB, and finally descending the WD cooling curve. These three classes of post-HB behavior have very different lifetimes, in the sense that the post-AGB stars are bright in the UV for a brief period ($\sim 10^3 - 10^4$ yr), the post-early AGB stars are UV-bright for a longer period ($\sim 10^4 - 10^5$ yr), and the AGB-Manqué stars are UV-bright for very long periods ($\sim 10^6 - 10^7$ yr). The HB phase itself lasts $\sim 10^8$ yr, and so the presence of hot HB stars in a population, combined with their long-lived UV-bright progeny, can produce the strong UV upturn seen in the most massive, metal-rich ellipticals (see Dorman, O'Connell, & Rood 1995 and references therein). In galaxies with a weak UV upturn, a significant fraction of the far-UV flux can theoretically come from post-AGB stars (see Brown et al. 1997), and in the weakest UV upturn galaxies – such as M32 – the spectra alone do not require the presence of a hot HB.

The ZAHB is not only a sequence in effective temperature: it is also a sequence in mass (see Dorman, Rood, & O'Connell 1993). For $T_{\rm eff} \gtrsim 6000$ K, a small change in envelope mass ($\lesssim 0.1\ M_\odot$) corresponds to a large change in $T_{\rm eff}$ ($\Delta T_{\rm eff} \gtrsim 10,000$ K), assuming solar abundances. Because the main-sequence turnoff (MSTO) mass decreases as age increases, the ZAHB will become bluer as a population ages, assuming all other parameters (e.g., mass loss on the red giant branch, metallicity, helium abundance, etc.) remain fixed. Note that this does not necessarily imply that age is the "second parameter" of HB morphology (e.g., Fusi Pecci & Bellazzini 1997; VandenBerg 1999; Sweigart 1999). The assumed first parameter of the HB morphology debate is metallicity; the HB becomes bluer at lower metallicity, assuming all other parameters (age, mass loss, etc.) remain fixed. This is due to two reasons. First, the MSTO mass at a given age is lower at lower metallicity, because a metal-poor star is more luminous (and thus shorter-lived) than a metal-rich star of the same mass. Second, as the metallicity decreases, the envelope opacity decreases, leading to a higher effective temperature on the HB. In short, HB morphology tends to become bluer at lower metallicity and higher ages, but other parameters may also play a role (rotation, He abundance, deep mixing, etc.). Although HB morphology in globular clusters (GCs) tends to become redder at increasing metallicity, there are examples of relatively metal-rich GCs with extended blue HBs (e.g., Rich et al. 1997), leading to the "second parameter" debate. Although elliptical galaxies should not be considered as overgrown globular clusters, they are generally believed to be metal-rich, old populations, and thus the presence of a hot HB in M32 can provide further insight into the production of blue HBs.

M32 has been the subject of several UV imaging programs with the Hubble Space Telescope (HST). The earliest of these observations (King et al. 1992; Bertola et al. 1995) were taken with the Faint Object Camera (FOC) before the correction of the spherical aberration, and were subject to large photometric uncertainties due to the calibration and aperture corrections. After the HST refurbishment with COSTAR, Brown et al. (1998) also observed M32 with the FOC, and detected the UV-bright post-HB phases of stars descended from the hot HB; although the calibration was improved in these later observations, the FOC was still subject to considerable uncertainties, such as an unexplained format dependence to the photometric zero points, and red leak. Here, we describe the deep UV imaging of M32 performed with the Space Telescope Imaging Spectrograph (STIS), a 2nd-generation HST instrument with a vastly improved performance and calibration. Our image is sufficiently deep to reach the HB at temperatures hotter than 8500 K, and in fact does reveal the presence of these stars, providing the first direct detection of hot HB stars in an elliptical galaxy. We interpret our data with a new set of evolutionary tracks, and compare our results to expectations from canonical tracks in the literature.

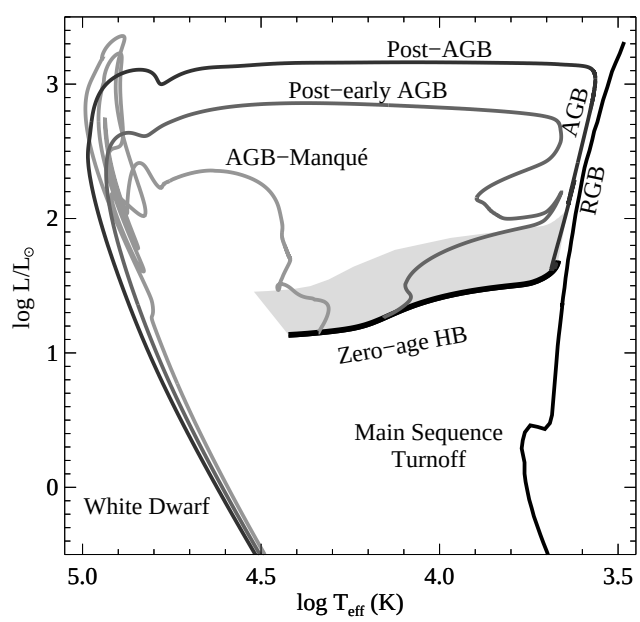

FIG. 1– The three classes of post-HB evolution arising from different ranges of effective temperature and envelope mass on the zero-age HB. The tracks shown assume solar metallicity and helium abundance, and are from our own calculations (see §6.3.1). For populations older than 1 Gyr, the HB phase (light grey) is brighter than the main sequence turnoff, which also contributes to the flux in the near-UV.

TABLE 1: Near-UV Photometric Catalog (abridged)

x (pix)	y (pix)	STMAG (mag)	error (mag)	region (#)	RA[a] (J2000)	Dec[a] (J2000)
38.6	112.9	25.64	0.11	1	0:42:40.4795	40:51:39.109
39.0	578.3	26.41	0.15	1	0:42:41.3862	40:51:34.325
39.2	199.4	27.33	0.40	1	0:42:40.6486	40:51:38.233
...	...	...	...	...	...	...
354.9	821.3	22.39[b]	0.02	3	0:42:42.1502	40:51:38.900
355.8	620.1	26.44	0.24	3	0:42:41.7592	40:51:40.992
...	...	...	...	...	...	...

[a]Note that the relative astrometry is quite accurate (tenths of a 0.025″ STIS pixel), but the absolute astrometry is subject to a ∼1″–2″ uncertainty (associated with the position of the guide stars).
[b]Stars associated with planetary nebulae in our field. Note that one of the four PNe in our field is at the edge of the frame and is thus not included in the catalog.

2. OBSERVATIONS

STIS observed M32 on 19 October and 21 October 1998, with four exposures on each day; the total exposure of the summed images is 22962 sec. The combined image, shown with a logarithmic stretch to enhance the faint stars, is shown in Figure 2. The data were taken with the near-UV multi-anode microchannel array (NUVMAMA), using the crystal quartz filter (F25QTZ); the filter blocks light shortward of 1450 Å and thus reduces the sky background from terrestrial airglow lines of O I and Lyman α. The long wavelength cutoff of the bandpass is 3500 Å, due to the sensitivity of the detector, and red leak at longer wavelengths is minimal (Baum et al. 1998). The STIS MAMAs are photon counters that register less than one count per incident cosmic ray; thus, cosmic ray rejection is not required, as it is with CCD imaging (where an incident cosmic ray causes a massive many-count "hit"). A full description of the instrument and its capabilities can be found in Woodgate et al. (1998) and Kimble et al. (1998).

The $25'' \times 25''$ (1024×1024 pixel) field was centered 7.7″ south of the M32 center, in order to overlap with earlier FOC UV imaging of M32 (Brown et al. 1998), to allow imaging in regions of lower diffuse galaxy background while still including the center of the galaxy, and to place the field farther from M31. The images were dithered between three positions along the X/Y diagonal of the detector: $+0.23''/+0.23''$, $0''/0''$, and $-0.23''/-0.23''$. Given the plate scale of 24.465 mas pix^{-1}, these offsets were equivalent to shifts of ≈9 pixels along each axis of the detector, which is useful for smoothing out small-scale variations in detector sensitivity. A small fraction of the field near the detector edge is occulted by a scattered-light mask very close to the focal plane: the lower right corner (≈9000 pixels), the upper right corner (≈2700 pixels), the bottom 20 rows, the first 8 columns, the top row, and last 4 columns. Although the mask slightly decreases the field of view, it does not vignette stars in the remainder of the field, and it does allow an accurate characterization of the dark counts in the data.

The STIS focal plane is tilted with respect to the detector when in imaging mode (STIS is optimized for spectroscopy). Thus, the PSF changes in shape and width as one moves from left to right in the field, and it also changes in time due to telescope breathing. Our final summed image averages over time to produce a PSF that is very nearly circular in the left half of the image, and noticeably elliptical in the right half of the image. Our detection limits are driven by the combination of both focus and galaxy background. In this image, the focus is best where the diffuse background from the core of M32 is faintest. This combination makes the limiting sensitivity significantly non-uniform over the summed image, but provides the deepest possible sensitivity in the well-focussed portions of the image. An elliptical Gaussian fit to isolated bright stars in the field has a FWHM range of 2.42–3.96 pix (0.06–0.1″), and an axial ratio range of 0.64–0.95.

We detect ∼8000 stars in the near-UV. Because the image contains $\approx 2.4 \times 10^5$ resolution elements (in the regions where we are actually cataloging stars), this is obviously a crowded field, with an average of one star per 30 resolution elements; near the M32 center, the crowding is severe, with one star per 12 resolution elements, but farther from the center it drops to one star per 63 resolution elements. The combination of this crowding with the variable PSF and the variable galaxy background makes photometry difficult, but not impossible, as we will discuss below.

Although the internal interstellar extinction within M32 is unknown, it is presumably small in comparison to the Galactic foreground extinction, thought to be anywhere in the range $0.035 \leq E(B-V) \leq 0.11$ mag (Tully 1988; McClure & Racine 1969; Burstein et al. 1988; Ferguson & Davidsen 1993; Burstein & Heiles 1984). For the purposes of this paper, we assume $E(B-V) = 0.11$ mag when comparing the data to the predictions of stellar evolutionary tracks, corresponding to 0.8 mag of extinction in the STIS bandpass.

Of the ∼ 8000 stars resolved in the STIS image, four of the brightest roughly coincide with the positions of the only known planetary nebulae (Ciardullo et al. 1989) in this field. Specifically, if one takes their positions in the SIMBAD database, there is a very bright star in the STIS image approximately 1″ west of each position, implying that there is a global offset between the astrometry of our image and that of the planetary nebulae. These stars are flagged in our catalog (Table 1, available from the CDS), and their positions are marked in Fig 3.

3. DATA REDUCTION

We reduced the raw images via the CALSTIS package in IRAF, including an updated pixel-to-pixel flat field file. Two steps in the reduction were done outside of CALSTIS: geometric correction was applied during the final combination via the IRAF DRIZZLE package, and dark subtraction was performed by subtracting a scaled and flat-fielded dark image from each data frame, with the scaling determined from the occulted right-hand corners of the detector. All frames were cross-correlated to provide accurate relative shifts. The calibrated frames were then drizzled to a 1060×1060 pixel image that included the data from all dither positions. The resulting image has a narrow strip of underexposed pixels along the edges, due to the dither

Figure 2 will be published as a color plate in ApJ.
It is too large to distribute in Postscript format.
A reduced−quality JPEG file (fig2.jpg) is available from
http://omri.pha.jhu.edu/~tbrown/m32nuv
The site also includes this page of the preprint with
the plate incorporated.

FIG. 2.— This false-color image of the M32 center uses a logarithmic scaling to enhance the faintest stars on the HB. The STIS field is $25'' \times 25''$, and the combination of the dithered positions have been summed onto a 1060×1060 pixel image (cropped to 1024×1024 pixels here). The occulted portions of the image are due to a scattered light mask, and vignetting is negligible.

TABLE 2: Photometry

region	x-position[a] (pix)	FWHM[b] (pix)	resolution elements	detected stars	fraction of near-UV flux resolved[c]	resolved fraction ≥ 25.5 mag[d]
1	37–141	2.68	30806	556	0.33	0.17
2	142–341	2.52	63677	1008	0.19	0.11
3	342–541	2.62	59818	1316	0.13	0.09
4	542–741	3.00	44864	2150	0.11	0.10
5	742–941	3.43	27366	2226	0.10	0.11
6	942–1037	3.62	13035	765	0.09	0.10

[a]Each region extends the full height of the image, excluding occulted detector areas and a $4'' \times 2.7''$ ellipse centered on M32. The galaxy center is at $(x,y) = (842.7, 392.7)$.
[b]This is the average FWHM of a Gaussian fit to the stars in each region, and is used for object detection.
[c]From all detected stars in the uncorrected catalog, and assuming a sky background of 9×10^{-4} cts sec^{-1} pix^{-1}.
[d]From the corrected luminosity function, assuming a sky background of 9×10^{-4} cts sec^{-1} pix^{-1}.

pattern. This strip is scaled correctly to account for the smaller exposure time, but thus has higher noise than the fully exposed area of the image. Stars in the underexposed strip are not included in our catalog, and this strip was not included in the Monte Carlo simulations discussed in §4.2 and §4.3.

The drizzle "dropsize" (also known as pixfrac) was 0.1, thus improving the resolution over a dropsize of 1.0 (which would be equivalent to simple shift-and-add). This small dropsize does not cause problematic "holes" in the final image, because the pixel scale was unchanged; it is thus equivalent to interlacing the individual frames. In the final image, pixels outside of the dither pattern or occulted are set to a count rate of zero. The pixel mask used in the drizzle for each input frame included the occulted regions of the detector, a small number of hot pixels, and pixels with relatively low response (those with values ≤ 0.75 in the pixel-to-pixel flat field).

4. PHOTOMETRY

4.1. *PSF Fitting*

Because the M32 image is fairly crowded, there are two obvious options for performing photometry: PSF fitting or small-aperture photometry. However, the PSF also varies strongly with position in the image, and so the aperture correction for small-aperture photometry would be a strong function of position, possibly introducing systematic errors in our catalog. We felt that PSF fitting offered the most accuracy for these data. As an initial estimate of the PSF variation, we used the IRAF routine FITPSF to fit an elliptical Gaussian to 180 of the brightest isolated stars in the image. The result defined a map of the Gaussian semi-major axis width as a function of position in the image. The map confirmed that the PSF varies as a function of horizontal position.

For our PSF fitting, we used the January 1998 version of the DAOPHOT-II package (Stetson 1987). The software allows calculation of relative photometry with a variable PSF defined by the user. Our iterative procedure was similar to that described in the User's Manual, to which we refer interested readers for details. However, because the PSF and the diffuse background from unresolved stars both vary with position, we chose to perform our photometry on six image regions (defined in Table 2). Object detection and PSF fitting for each region were done with the region boundaries extended 50 pixels into the neighboring regions, to avoid edge effects with stars near the region boundaries. Thus, at each region boundary, there is a 100-pixel wide strip where stars are fit twice, and we use this

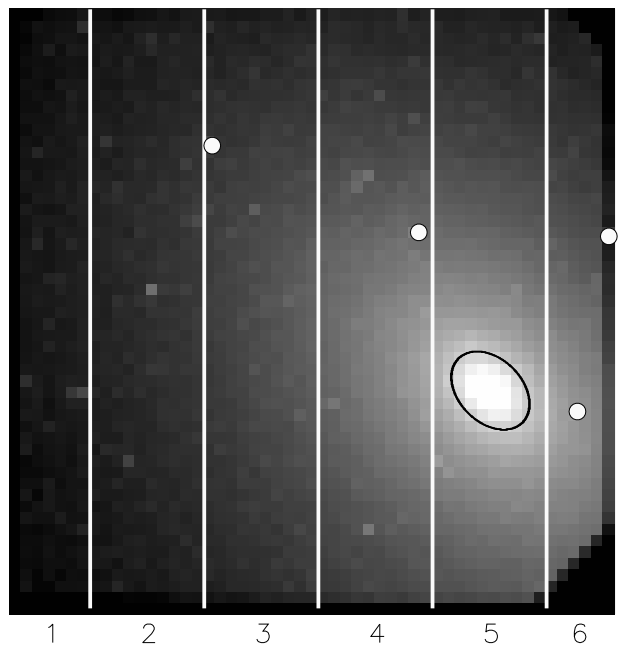

FIG. 3– This schematic of the STIS image shows some of the details of the reduction discussed in the text. The six labeled vertical strips are the regions used for PSF fitting and photometry. Stars were rejected from the catalog within the black ellipse in the center of the galaxy. White circles show the positions of the bright stars that correspond to the positions of the four known planetary nebulae in our field; from left to right, they are: Ford-NGC221-21, Ford-NGC221-23, Ford-NGC221-27, and Ford-NGC221-24.

overlap to put the stars in each region on the same magnitude system (see below). Each region spanned the entire height of the image, with region 5 encompassing the center of the galaxy. From our initial map of elliptical Gaussian fits, we determined the "average" width of a star in each region (Table 2), and used this width for object detection. DAOPHOT convolves an image with a Gaussian as part of its object detection algorithm, but the user must specify a constant width for each image under consideration. Thus, our use of a different width for each region allows optimization of the object detection.

To determine a variable PSF for each region, we first subtracted a median-filtered image from the data to remove the varying galaxy background. We found that this subtraction prevented a spurious biasing of the PSF wings; fitting the PSF with

the galaxy background intact incorrectly tilts the PSF wings along the slope of the galaxy background. Our PSF in each region is a Moffat function with a lookup table of empirical corrections. The PSF in each region was allowed to vary linearly with position. Although DAOPHOT allows quadratic variations in the PSF, our PSF subtraction was worsened when we attempted to allow such higher order variation. The PSF determination was done though an interactive selection of the brightest isolated stars, with iterations to subtract the PSFs of the neighboring stars, as described in the manual for the software. The PSF was defined with a radius of 10 pixels.

After determining a variable PSF for each image region, we performed object detection and PSF fitting on the data, again using the regions defined in Table 2 (but without the galaxy background subtraction). To maintain positional consistency, we did not actually extract the regions from the image; we simply set those pixels outside of a given region to a "bad" pixel value, thus producing a mask for each region. In region 5, which contains the M32 center, we also masked off a $0.75'' \times 0.5''$ ellipse aligned to the axis of M32 (45° counterclockwise from the +y axis of the image), in order to prevent an unnecessary biasing of the "sky" level, and because the very center appeared hopelessly crowded. In the final catalog, we actually rejected stars in a larger $4'' \times 2.7''$ ellipse, after reevaluating the severity of the crowding. We set the detection threshold to 5 σ; setting a lower threshold produces many false detections, because the diffuse background varies with position, even within the subsections we defined. The detection algorithm convolves the image with a symmetrical Gaussian with a width equal to the FWHM of the PSF, and then looks for deviations above the local sky background (see Stetson 1987 for a complete description). We set the "roundness" and "sharpness" criteria to twice their default values, because the STIS PSF is not symmetrical and there is no need to reject cosmic rays in STIS MAMA images. After a first pass of object detection and PSF fitting, the star-subtracted image is used for a second pass at object detection, and the final combined catalog is used for a second pass of PSF fitting. The PSFs were fit to the stars using a fitting radius of 3 pixels and a sky annulus spanning 8–15 pixels in radius. The DAOPHOT package is capable of iteratively solving for the sky under the star itself (hence the inner radius of the sky annulus falls within the PSF radius).

DAOPHOT calculates the *relative* magnitudes of stars in each region. Putting all of the stars in each region on the same system required several additional steps. The PSF in region 2 is the most circular and has the smallest FWHM. We performed aperture photometry on the 10 brightest stars in region 2, with the aperture varying from 3–10 pixels in radius. Next, we performed the same aperture photometry on the quasar in the Hubble Deep Field South (HDF-S) near-UV image (Gardner et al. 1999). The encircled-energy variation with aperture size in our M32 image was nearly identical to that of the quasar. We then used the quasar (with object masking for the other galaxies in the HDF-S) to determine an aperture correction of 0.524 mag for a 3-pixel radius aperture, and used this aperture correction to calculate the corrected magnitudes of the 10 bright stars in M32. This then determined the zero-point for the DAOPHOT magnitudes in region 2. Next, we used the 100-pixel-wide overlaps at region boundaries (see above) to place all of the stars on the same magnitude system as region 2; the photometry in each region was shifted by less than 0.1 mag as part of this correction. Our magnitudes are specified in the STMAG system:

$$m = -2.5 \times \log_{10} f_{\lambda} - 21.10$$

$$f_{\lambda} = \text{counts} \times \text{PHOTFLAM}/\text{EXPTIME}$$

where EXPTIME is the exposure time, and PHOTFLAM is 5.588×10^{-18} erg s^{-1} cm^{2} Å^{-1} / (cts s^{-1}).

The entire photometric catalog (Table 1) is available from the CDS. Table 3 shows the raw (uncorrected) luminosity functions in each region.

TABLE 3: Uncorrected Luminosity Functions

	No. of stars in region					
mag	1	2	3	4	5	6
21.0	0	0	0	0	1	0
21.5	0	1	0	2	2	0
22.0	0	0	1	4	5	2
22.5	1	2	2	4	1	0
23.0	2	1	2	7	6	1
23.5	1	3	4	10	16	5
24.0	6	9	12	29	69	16
24.5	7	7	31	58	197	31
25.0	14	43	95	248	403	146
25.5	66	196	328	588	649	271
26.0	110	306	416	706	555	214
26.5	154	255	323	388	254	69
27.0	139	135	92	102	67	10
$\geq$ 27.5	56	50	10	4	1	0

4.2. *Completeness*

In the deepest regions of the image, we are detecting stars down to 28 mag. However, the catalog becomes seriously incomplete well before this point is reached, and the completeness varies from region to region. To determine the completeness as a function of magnitude in each region, we ran thousands of Monte Carlo simulations, using the DAOPHOT package and our own IDL-based programs. For each region, 10 stars at a given magnitude were placed within the region at random positions, using the variable PSF for that region, and including Poisson noise in the artificial stars. The entire object detection and PSF fitting process was then performed, and the catalog was checked to see if the stars were recovered. This process was then repeated until the calculated completeness was deemed well-determined, with the criteria that the calculated completeness not change significantly (by $>$1%) over many runs. Because we only add 10 stars per simulation, we are not significantly affecting the crowding in the data (which contains hundreds of stars in each region). Table 4 lists the completeness versus magnitude for each region. Note that the object detection is done with a Gaussian convolution of constant width (specified in Table 2), while the artificial stars are created using the empirically-corrected Moffat function that was determined from the STIS data (and significantly different from a Gaussian); thus, the completeness determination is not a circular process, and it does accurately model the true detection process. Because the strength of the galaxy background has a strong influence on the completeness, the completeness is best in region 1, even though the PSF is sharpest in region 2.

To ensure that inaccuracy in our variable PSF template does not skew the determination of the completeness, we recalculated a set of completeness simulations using smoothed PSFs for the artificial stars. Because these test PSFs were not as

strongly peaked, they could possibly reduce the detectability. We first smoothed the true PSF with a kernel that redistributed 10% of the flux in each pixel to its 8 neighbors, and then with a kernel that redistributed 20% of the flux in each pixel to its 8 neighbors. The artificial stars were then added to the data with Poisson noise, as before. Although we used these *altered* PSFs to generate the artificial stars in the Monte Carlo simulations, we used the *true* PSF for the PSF fitting, thus simulating a mismatch between the object PSF and the fitted PSF. Fortunately, the recalculated completeness versus magnitude remained virtually unchanged when these altered PSFs were used, thus demonstrating that small errors in the assumed PSF do not significantly affect the completeness determination.

TABLE 4: Completeness in Near-UV Number Counts

	region					
mag	1	2	3	4	5	6
21.5	1.00	1.00	1.00	1.00	0.91	0.98
22.0	1.00	1.00	1.00	1.00	0.90	0.97
22.5	0.99	0.99	1.00	0.98	0.88	0.96
23.0	1.00	0.99	0.99	0.98	0.89	0.96
23.5	0.99	0.99	0.98	0.96	0.85	0.94
24.0	0.99	0.98	0.98	0.95	0.83	0.92
24.5	0.97	0.97	0.96	0.93	0.81	0.89
25.0	0.97	0.96	0.95	0.87	0.73	0.77
25.5	0.96	0.96	0.92	0.79	0.55	0.60
26.0	0.92	0.87	0.71	0.48	0.29	0.22
26.5	0.68	0.46	0.25	0.14	0.08	0.04
27.0	0.24	0.11	0.05	0.04	0.02	0.01
27.5	0.06	0.02	0.01	0.00	0.01	0.00

4.3. *Spurious Sources*

Because we set the DAOPHOT detection threshold a bit higher than the nominal value of 4 σ, we do not expect many spurious sources to be detected in the data, except perhaps in region 5, where the galaxy background varies strongly with position. However, to quantify exactly how many spurious detections we have in our catalog, we ran another series of Monte Carlo simulations.

Each simulation starts with a model of the diffuse light, derived by taking the median of the true image, and assuming elliptical isophotes to handle edge effects and occulted regions. This galaxy model was then used to create a starless simulation of each of the eight STIS exposures, by dithering the model, scaling by the exposure time, applying detector occultation in the corners and along the edges, adding dark counts, and adding Poisson noise. The eight simulated exposures were then drizzled into one image, in the same manner as the true data. This image matched the noise characteristics of the actual data in the areas free of point sources. Finally, two passes of object detection and PSF fitting were then applied, again following the actual data reduction described above. The process was repeated 100 times for each region, to determine the average number of spurious sources one would expect as a function of magnitude in each region. The results are tabulated in Table 5.

As expected, spurious sources do not significantly contaminate our catalogs where the completeness is larger than 10%. The number of spurious sources also begins to drop at the faintest magnitudes, because such stars fluctuate below the 5 σ detection limits.

TABLE 5: Spurious Source Contamination

	region					
mag	1	2	3	4	5	6
23.5	0	0	0	0	0	0
24.0	0	0	0	0	1	0
24.5	0	0	0	0	3	0
25.0	0	0	0	0	14	0
25.5	0	0	0	1	42	1
26.0	0	0	0	9	88	15
26.5	0	0	1	62	120	41
27.0	3	6	20	55	36	9
27.5	17	21	12	1	0	0

4.4. *Systematic Errors*

4.4.1. *Comparison with FOC*

UV imaging of the evolved stellar populations in M31 and M32 has been subject to considerable calibration problems, and the story of these problems underscores the need for faint UV standards appropriate for direct imaging with today's sensitive instruments. King et al. (1992) imaged M31 and M32 with the pre-COSTAR FOC and assumed that the FOC sensitivity was degraded to 80% of nominal. Bertola et al. (1995) imaged the same galaxies, and their adoption of a degraded FOC sensitivity (at 30–40% of nominal in the UV) implied even brighter UV luminosities for these stars. Both sets of pre-COSTAR data required large aperture corrections ($>$ 2 mag) because of the spherical aberration present in the first-generation instruments. Subsequent recalibration of the FOC showed that the UV sensitivity of the King et al. (1992) data was supposedly at 144% of nominal, due to the format dependence of the FOC zero-points (Greenfield 1994). After refurbishment of HST, Brown et al. (1998) used the FOC to image M31 and M32, and found that its nominal calibration implied that the stars common to both the Brown et al. (1998) data and the King et al. (1992) data were 1.9 mag fainter than previously thought by King et al. (1992); this discrepancy dropped to 1.2 mag once the format dependence of the FOC zero-points was included in the King et al. (1992) magnitudes. Brown et al. (1998) attempted several cross-checks of the refurbished FOC calibration, and found inconclusive evidence for 0.25 mag systematic shifts to the zero points, in the sense that these UV-bright stars could be 0.25 mag brighter than implied by the nominal calibration of the refurbished FOC. However, these checks were done via comparison to spectra and galaxy photometry – no images of globular clusters or isolated stars were available in the appropriate imaging modes.

Our new STIS observations of M32 include the entire field observed by Brown et al. (1998) with the FOC. Given the STIS magnitudes (m_{NUV}) and the FOC magnitudes (m_{F175W} and m_{F275W}) for these stars, color-color diagrams of $m_{NUV} - m_{F175W}$ versus $m_{F175W} - m_{F275W}$ and $m_{NUV} - m_{F275W}$ versus $m_{F175W} - m_{F275W}$ demonstrate that the FOC magnitudes in Brown et al. (1998) should be revised 0.5 mag brighter than listed in the Brown et al. (1998) catalog, assuming that the observed stars span a range of effective temperature from 8000–30000 K. This revision would further reduce the discrepancy between the Brown et al. (1998) data and the King et al. data (1992) to 0.7 mag, and so this remaining discrepancy might be due to the large aperture corrections in the pre-COSTAR data. However, we note that this means the UV-bright stars in the King et al. (1992) data are 1.4 mag fainter than originally thought by King et al. (1992); thus, these stars are not bright enough to be post-

AGB stars (the interpretation of King et al. 1992 and Bertola et al. 1995), and are consistent with post-HB evolution from the hot end of the HB, as described in Brown et al. (1998). Shifting the stars in the Brown et al. (1998) color-magnitude diagrams by 0.5 mag in both filters does not move the bulk of the stars onto post-AGB tracks.

4.4.2. *Comparison with WFPC2*

The STIS photometric calibration is reliable at the 0.15 mag level, according to the STScI documentation (Baum et al. 1998); this is considerably more secure than that of the earlier generation instruments on the HST. At the time of this writing, new calibration efforts at STScI will revise the photometric zero-points slightly, and adaptation of these new zero points would make our stars up to 0.07 mag brighter. Our analysis is not sensitive to such a small shift in sensitivity, and so we do not adopt the revision.

Our own consistency check, using STIS & WFPC2 UV images of the globular cluster NGC6681, confirms the photometric accuracy of STIS. In the UV, this GC is not crowded and does not have an underlying galactic background; it gives a much better sensitivity check than the data available for checks of the FOC calibration. STIS imaged NGC6681 with the near-UV crystal quartz filter and the far-UV SrF_2 filter (m_{FUV}); 22 bright isolated stars are available in the field for accurate photometry. The same field was also observed by WFPC2 using the F160BW filter (m_{F160BW}). The F160BW filter has very low throughput, but very little red leak. These bright stars have $\lesssim 0.05$ mag statistical errors in the WFPC2 frame, and $\lesssim 0.01$ mag statistical errors in the STIS frames. Color-color diagrams of $m_{FUV} - m_{F160BW}$ versus $m_{FUV} - m_{NUV}$ and $m_{NUV} - m_{F160BW}$ versus $m_{FUV} - m_{NUV}$ are consistent at the 0.1 mag level when compared to expectations for stars spanning a range of effective temperature 8000–30000 K. The expected colors were calculated by folding the synthetic spectra of Kurucz (1993) through the bandpasses of the IRAF SYNPHOT package.

4.4.3. *Comparison with IUE*

The center of M32 was observed by IUE at low signal-to-noise (S/N) in the wavelength range 1150–3200 Å, thus covering most of the STIS bandpass. We compare the STIS image to a composite UV+optical aperture-matched spectrum (Calzetti, private communication); because the red leak in STIS is so low, the optical portion of the spectrum has little affect on the analysis, but is included for completeness. We show our bandpass and this spectrum in Figure 4.

The IUE aperture was a $10'' \times 20''$ oval. Because M32 is not centered in the STIS image, we must define two regions in the STIS field that can be used for comparison to IUE: a $10'' \times 10''$ square centered on the M32 nucleus, and an adjacent semicircle with a radius of $5''$. The addition of the flux in the square with twice that of the semicircle is equivalent to the IUE aperture.

Within this artificial aperture, STIS measures a dark-subtracted count rate of 3228 cts sec^{-1}. A template of the "average" sky background, available from the STScI web page, shows that $\sim$275 cts sec^{-1} of this could be from the sky background, and so the sky-subtracted count rate measured by STIS in an IUE-equivalent aperture is $\sim$2950 cts sec^{-1}. Folding the composite IUE+optical spectrum of IUE through the STIS bandpass (via the IRAF package SYNPHOT) predicts 2738 cts sec^{-1}, within 10% of the actual value measured by STIS. Given the uncertainty in the true sky level, the IUE and STIS observations are in acceptable agreement.

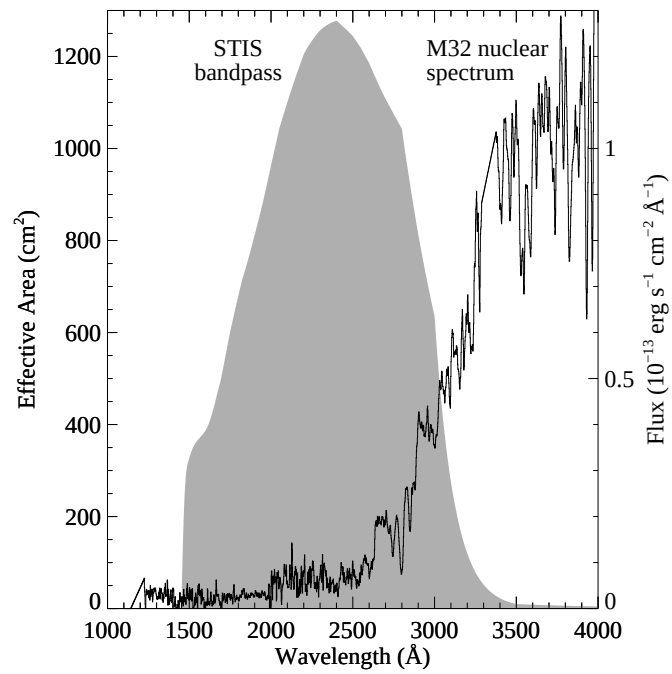

FIG. 4– The nuclear ($10'' \times 20''$) spectrum (solid; Calzetti, private communication), an aperture-matched splice of IUE and ground-based data, demonstrates that the STIS bandpass (grey shaded) incorporates flux from both the short-wavelength UV upturn population and the cooler stars in earlier evolutionary phases. Given that these cooler populations are several magnitudes fainter than our detection limit in this bandpass, they contribute to the diffuse background in our data.

5. RESOLVED FRACTION OF NEAR-UV LIGHT

Because the STIS image is the deepest near-UV image of M32 to date, we compare the resolved flux with the total flux in the STIS bandpass. The fraction of resolved flux varies with position in the image: a much larger fraction of the near-UV light is resolved into stars as one moves away from the M32 center. In Table 2, we show the fraction of M32 flux within the STIS bandpass resolved into stars, for each of the 6 regions defined in the table. In each region, we subtract a sky background of 9×10^{-4} cts sec^{-1} pix^{-1}, which comes from the "average" sky template available on the STScI web page, folded through the SYNPHOT package bandpass. We then calculated the resolved fraction via two different methods. In the first method, we simply took the catalog of stars for that region, summed the flux from those stars, and divided by the total flux in that region. This did not assume any completeness correction, nor did it reach a uniform depth as a function of position in the image. In the second method, we summed the flux in the corrected luminosity function for those magnitude bins ≥ 25.5 mag (i.e., better than 50% completeness everywhere), and then divided by the total flux in that region. Thus, this second method reaches a uniform limiting magnitude across the image. We resolve $\sim$10% of the near-UV flux in most of the image, and about a third of the near-UV flux in the deepest section. We do not expect to resolve all of the flux, because a considerable fraction of the light in our bandpass comes from the cooler populations that are below our detection limits in the near-UV (see Figure 4). It would take *much* deeper imaging in this bandpass, at much higher resolution, to resolve significantly more flux, be-

cause the main sequence turnoff is several magnitudes below the HB (see Figure 1).

6. COMPARISON WITH EVOLUTIONARY TRACKS

6.1. *The Stellar Evolutionary Flux*

Before comparing our luminosity functions to the expectations from stellar evolutionary tracks, it is important to place constraints on the population under consideration. We cannot have an arbitrary number of stars leaving the MSTO and eventually passing through the HB phase; the bolometric luminosity of the population and the stellar lifetimes constrain the number of stars in a given evolutionary phase (Greggio & Renzini 1990; Renzini 1998). The stellar death rate, or stellar evolutionary flux (SEF), is given by the relation SEF $= B(t)L_T$, where L_T is the total bolometric luminosity of the population, and $B(t)$ is the specific evolutionary flux. The specific evolutionary flux is a weak function of age, and for a population of age ~ 10 Gyr, $B(t) \cong 2.2 \times 10^{-11}$ stars yr^{-1} $L_\odot^{-1}$ (Renzini 1998).

The section of the STIS image most appropriate for an analysis of the HB is the sum of regions 1, 2, and 3 (see Table 2). Restricting our comparison to this deep portion of the STIS image avoids the complications of crowding, systematic errors due to a steeply varying background, and seriously incomplete photometry at the magnitudes of interest (~ 27 mag). We will refer to this section as R_{123}; the left and right edges of this section are $20''$ and $8''$ from the center of M32, respectively. Later analyses, especially if color information becomes available on these stars, may include the full catalog, with some appropriately bright magnitude cutoff in the regions that are very crowded. The luminosity function (LF) in R_{123} is shown in Figure 5. Two key features of this LF, which will be addressed later, are the lack of stars brighter than 22 mag and the large number of stars near 26 mag.

We determined the bolometric luminosity in R_{123} in the following manner. First, we registered the archival WFPC2 F555W image (HST Guest Observer ID No. 5236) to our STIS field and summed the count rate in R_{123} to obtain 2.62×10^4 cts sec^{-1}. The corresponding M_{F555W} is 11.44 mag on the STMAG system. Conversion to Johnson V involved a small, color-dependent correction; we used the M32 nuclear spectrum to derive an offset of -0.03 mag, giving $m_V = 11.41$ mag. Assuming a foreground extinction of $E(B-V) = 0.11$ mag with $R_V = 3.1$ (see §2) and a distance modulus of 24.43 mag gives $M_V = -13.36$ mag. Worthey (1994) gives bolometric corrections for passively evolving populations as a function of age and metallicity; for these purposes, we assume an age of 8 Gyr and solar metallicity (see Grillmair et al. 1996; Da Costa 1997 and references therein), giving $BC_V = -0.875$ mag. Note that this parameter is sensitive to the assumed age and metallicity. At [Fe/H] = 0.0 and an age of 5 Gyr or 12 Gyr, BC_V is -0.768 or -0.963 mag, respectively; at 8 Gyr and [Fe/H] = -0.25 or +0.25, BC_V is -0.679 or -1.130, respectively. Using our assumed metallicity and age, the bolometric luminosity is $3.92\times10^7\,L_\odot$ in R_{123}, and thus the associated SEF is 8.62×10^{-4} star yr^{-1}. This is the upper limit we will place upon the number of stars entering the evolutionary tracks in the following discussion. Note that the SEF in the entire STIS image, which includes significantly more luminosity than that in R_{123}, is 4.18×10^{-3} star yr^{-1}, using the same calculations and assumptions.

In the subsequent discussion, we will translate tracks from the literature and from our own calculations into magnitudes in the STIS bandpass. These translations will be obtained from the solar-metallicity Kurucz (1993) synthetic spectra, interpolating in effective temperature from the grid points with the closest match in surface gravity and metallicity. We then assume a foreground reddening of $E(B-V) = 0.11$ mag, following the Cardelli, Clayton, & Mathis (1989) parameterization, and a distance of 770 kpc. Because we are comparing to the STIS data in 0.5 mag bins, our analysis is not very sensitive to these assumptions.

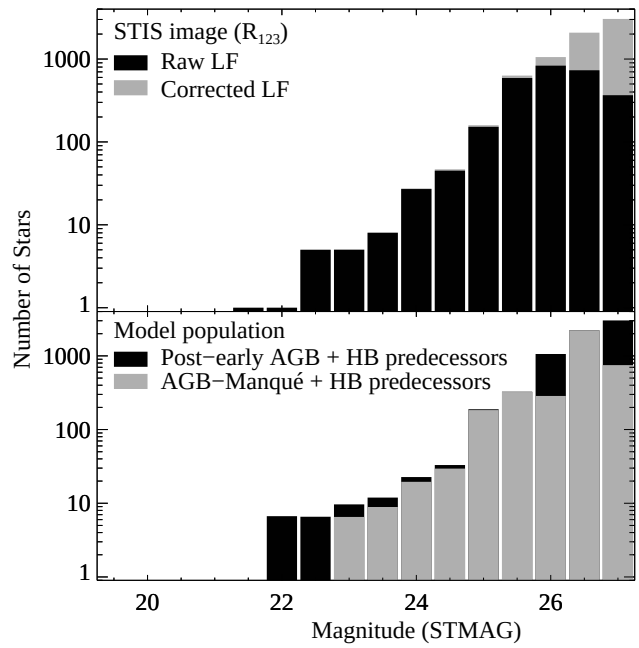

FIG. 5– The STIS luminosity function in the deepest half of the image (R_{123}) is shown with and without corrections for incompleteness in the number counts (top panel). A minority population of hot HB stars and their progeny (bottom panel; see §6.3) can easily explain the STIS luminosity function. This model population is comprised of the tracks listed in Table 8. Note the logarithmic scaling.

6.2. *Post-AGB Evolution*

At an age of 8 Gyr, the main sequence turnoff mass is $\sim 1.1\,M_\odot$ at solar metallicity (Bertelli et al. 1994), and the core mass of post-AGB stars is expected to be low ($\lesssim 0.6\,M_\odot$; Vassiliadis & Wood 1993). Assuming that the dominant population in M32 is at an age of at least 8 Gyr, most of the stars that leave the red end of the HB should pass through the post-AGB tracks of lowest mass in the compilations of Schönberner (1987) and Vassiliadis & Wood (1994). The luminosities of these stars as they cross the HR diagram from the AGB to the white dwarf cooling curve are listed in Table 6. We are comparing the STIS data to these tracks from the literature because they have been widely used; our own set of evolutionary models includes post-AGB behavior that produces very similar luminosity functions. Note that our post-AGB track shown in Figure 1 crosses the HR diagram at a very low-mass ($0.538\,M_\odot$), and is thus somewhat dimmer in luminosity than the tracks taken from the literature.

A post-AGB star should cross the HR diagram at a luminosity near that of the AGB tip luminosity. Several recent investigations of the AGB tip luminosity in M32 show there is a significant population of stars on the AGB at luminosities brighter than the tip of the red giant branch (RGB) (see Grillmair et

al. 1996 and references therein). However, earlier studies that found very bright AGB stars, like those associated with young populations, were apparently affected by crowding; instead, it appears that the bright AGB stars in M32 belong to a population of long period variables (LPVs) and blue-straggler progeny, like those found in the old metal-rich globular clusters 47 Tuc and NGC6553 (Guarnieri, Renzini, & Ortolani 1997; Renzini 1998; Grillmair et al. 1996). Note that in a solar-metallicity population of age 8 Gyr, the RGB tip lies at $log(L/L_{\odot}) = 3.2$ (Bertelli et al. 1994). The lack of bright AGB stars associated with young populations supports the premise that the majority of the post-AGB stars in M32 should be evolving along low-mass tracks (near this luminosity).

TABLE 6: Post-AGB Crossing Luminosities

Mass	$log(L/L_{\odot})$
H-burning 0.546 $M_{\odot}^{a}$	3.2
H-burning 0.569 $M_{\odot}^{b}$	3.5
H-burning 0.597 $M_{\odot}^{b}$	3.7
H-burning 0.633 $M_{\odot}^{b}$	3.9
He-burning 0.567 $M_{\odot}^{b}$	3.5
He-burning 0.600 $M_{\odot}^{b}$	3.6

[a]Schönberner (1987). A post-early AGB track just below the mass required for post-AGB behavior.
[b]Vassiliadis & Wood (1994).

Until the middle of this decade, post-AGB stars were thought to be predominantly H-burning (see Vassiliadis & Wood 1994 and references therein). H-burning post-AGB stars leave the AGB between He-shell flashes, while He-burning post-AGB stars leave the AGB near or during a flash, and the ratio of He-burning to H-burning lifetimes over the He-shell flash cycle was thought to be on the order of 20%. However, Vassiliadis & Wood (1994) suggested that at lower masses, the chance of producing a He-burning post-AGB star increased (see also Renzini & Fusi Pecci 1988; Renzini 1989). Post-AGB evolution remains as one of the least-understood phases of normal stellar evolution; more observational evidence is needed to determine the relative frequency of H-burning and He-burning tracks (see Dopita, Jacoby, & Vassiliadis 1992).

M32 has a very weak UV upturn, and thus, prior to our observations, the UV flux could theoretically be explained by low-mass post-AGB stars alone; no hot HB stars were required. We know that hot HB stars, if present, can only comprise a minority of the population, else the UV upturn in M32 would be considerably stronger; the elliptical galaxies with the strongest UV upturns only require $\sim 10\%$ of the SEF to pass through the hot HB and its descendants (Brown et al. 1997). We expect most of the stars in M32 to pass through the red end of the HB and the subsequent low-mass post-AGB tracks. While post-AGB stars evolve very rapidly through their UV-bright phases compared to the hot HB stars and their progeny (see §1), the low-mass post-AGB tracks nevertheless evolve slowly enough to produce dozens of stars at very bright magnitudes in the STIS bandpass. This is shown in Table 7, which shows the luminosity functions obtained by placing the entire SEF (determined for R_{123} in §6.1) into selected low-mass tracks from the literature. For comparison, we show the raw and corrected luminosity functions obtained in the deepest half of the STIS image, R_{123} (see §6.1). It is obvious from Table 7 that low-mass H-burning tracks suffer from two problems when trying to explain the STIS luminosity function: the models predict far too many stars at bright magnitudes ($\lesssim 23$ mag) and far too few stars at faint magnitudes ($\gtrsim 24$ mag), even when the faint magnitudes are not corrected for completeness. Low-mass He-burning post-AGB tracks fair somewhat better with the bright end of the STIS luminosity function, as they do not predict nearly as many bright stars, but these tracks still produce far too few stars at faint magnitudes. These He-burning tracks also produce a fairly bright local maximum in their luminosity functions (see Table 7) that is not seen in the STIS data, but the luminosity of this phase depends upon the mass and the details of the evolution. Thus this spike in the LF could be easily hidden in the STIS data if there was a small dispersion in post-AGB mass, centered at a low mass ($\lesssim 0.567\ M_{\odot}$).

The lack of UV-bright stars in the STIS data requires that the transition from the AGB to $T_{\rm eff} > 60000$ K occurs on a much more rapid timescale than predicted by the low-mass H-burning tracks, or, alternatively, that this transition be hidden by circumstellar dust produced during the preceding AGB mass-loss (see

TABLE 7: Comparison with Post-AGB Tracks

	Data		Theoretical Maximum Number of Post-AGB Stars				
mag	Raw LF regions 1+2+3	Corrected LF regions 1+2+3	0.546 $M_{\odot}^{a}$ H burning	0.569 $M_{\odot}^{b}$ H burning	0.597 $M_{\odot}^{b}$ H burning	0.567 $M_{\odot}^{b}$ He burning	0.600 $M_{\odot}^{b}$ He burning
20.0	0	0	0	0	1	0	0
20.5	0	0	0	6	2	1	0
21.0	0	0	0	4	0	1	2
21.5	1	1	54	3	1	1	1
22.0	1	1	40	2	1	1	4
22.5	5	5	30	2	1	2	14
23.0	5	5	23	2	0	2	2
23.5	8	8	24	2	1	29	2
24.0	27	27	29	2	1	4	1
24.5	45	47	26	2	1	4	1
25.0	152	159	26	2	0	3	1
25.5	590	631	16	1	1	3	1
26.0	832	1055	15	2	0	3	1
26.5	732	2079	22	7	1	11	4
27.0	366	3045	32	33	3	22	10

[a]Schönberner (1987). A post-early AGB track just below the mass required for post-AGB behavior.
[b]Vassiliadis & Wood (1994).

Figure 6). If the transition is only accelerated up to a somewhat cooler temperature (e.g., 30000 K or 50000 K), there will still be too many stars in the LF bins brighter than 23.5 mag. The pace of this transition is naturally increased by assuming post-AGB tracks of higher mass ($\gtrsim 0.6\ M_\odot$), but, as we stated above, the observational and theoretical evidence on the maximum AGB stellar luminosity seems to preclude this option. Furthermore, the AGB precursors of a population of stars this massive would produce an enormous amount of energy, leading to optical-infrared colors in disagreement with observations (Greggio & Renzini 1999). Circumstellar extinction, while having a strong effect in the UV, would also appear to be an unlikely candidate, considering the rapid thinning times for material surrounding post-AGB stars (Käufl, Renzini, & Stanghellini 1993; Brown et al. 1998), although we cannot rule out this alternative.

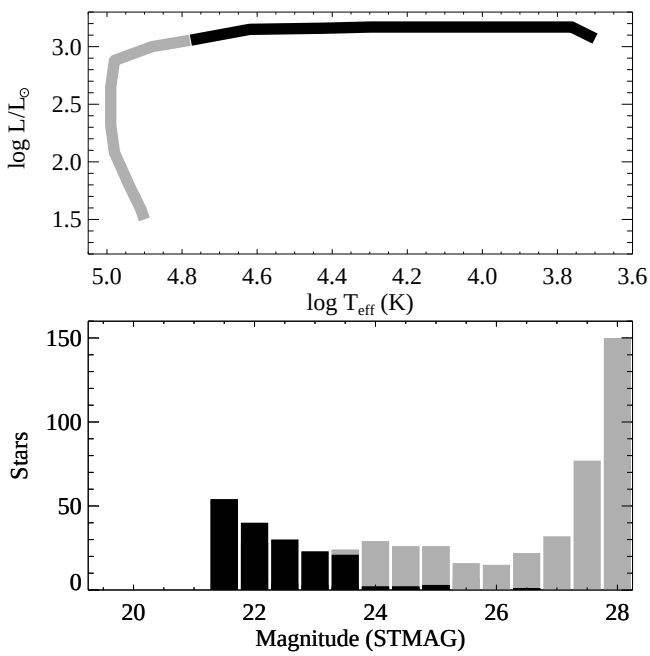

FIG. 6– The 0.546 $M_\odot$ H-burning track of Schönberner (1987), and the corresponding luminosity function from Table 7. The track and model luminosity function have been color-coded to demonstrate that the evolution up to T_{eff} = 60000 K causes the discrepancy with the STIS luminosity function (i.e., the dark segment of the track produces the dark portion of the luminosity function bins). If this evolution were more rapid or hidden, the lack of UV-bright stars in the STIS image would be explained.

The most likely explanation for the lack of bright stars is that most of the population evolves more rapidly from the AGB to high effective temperature than predicted by the tracks in Tables 6 and 7. This might occur if the final mass ejection on the AGB was triggered by a helium-shell flash which left the star out of thermal equilibrium. The post-AGB evolution would then take place on the more rapid thermal timescale, as argued by Käufl et al. (1993) and Greggio & Renzini (1999). Indeed, Table 7 already demonstrates that the discrepancy with the STIS data is greatly reduced if the stars evolve as He-burners. Note that the number of known planetary nebulae in the STIS field (four), combined with the stellar evolutionary flux for the entire STIS field (4.18×10^{-3} star yr^{-1}), implies that the planetary nebula phase only lasts for ~ 1000 yr. Although we might have an explanation for the lack of bright stars, there is no post-AGB track that can produce the thousands of stars on the faint end of the STIS luminosity function, and so we next explore the expectations from hot horizontal branch stars and their progeny.

6.3. *Hot HB stars*

As explained in §1, the HB phase (shown as a light grey region in Figures 1 and 7) lasts for $\sim 10^8$ yr, and the UV-bright post-HB lifetime for stars leaving the hot end of the HB is on the order of 10^7 yr. These long lifetimes in the UV suggest that hot HB stars and their progeny are much more likely to explain the STIS luminosity function, compared to the brighter short-lived post-AGB stars. We explore this possibility here, using our own calculations of HB and post-HB evolution.

6.3.1. *Models*

We have calculated a detailed grid of HB and post-HB sequences with solar metallicity and helium abundance, over a wide range in the HB mass, and for various rates of mass loss along the AGB. A fine spacing in the HB mass was used, in order to clearly define the changes in the HB morphology with mass, as well as the transition between the AGB-Manqué, post-early-AGB, and post-AGB evolution. Evolution was followed from the ZAHB until the luminosity fell below 0.1 $L_\odot$ along the white dwarf cooling curve. In a few cases, the models underwent a final helium-shell flash while descending the WD cooling curve, and such sequences were stopped if the flash convection reached into the hydrogen envelope.

In order to obtain a ZAHB model at the red end of the HB, we first evolved a 1 $M_\odot$ stellar model from the zero-age main sequence up the RGB, and then through the helium-core flash. The parameters of the initial main-sequence model were determined by calibrating the model on the sun; i.e., the main sequence helium abundance Y_{MS}, heavy-element abundance Z, and mixing-length ratio α were adjusted until the model matched the observed solar luminosity, radius, and Z/X ratio at a solar age of 4.6 Gyr. The parameters derived in this fashion are: $Y_{MS} = 0.2798$, $Z = 0.01716$, and $\alpha = 1.8452$. The helium abundance increased to 0.3003 during the first dredge-up along the lower RGB. Consequently, all of the HB and AGB sequences we have computed have the following envelope abundances: $Y = 0.3003$ and $Z = 0.01716$.

Mass loss was included during the RGB phase using the Reimers (1975) mass-loss formulation, with a mass-loss parameter η_R of 0.4. As a result, the mass decreased to 0.8269 $M_\odot$ by the time the model reached the ZAHB. The age at that time was 12.2 Gyr. The use of a somewhat different initial mass (corresponding to a somewhat different age) would have only a negligible effect on the core mass and envelope helium abundance of this ZAHB model. Thus our results do not depend significantly on the choice for the zero-age main sequence model.

Lower mass ZAHB models were then computed by removing mass from the envelope of the red ZAHB model described above. The lowest ZAHB mass considered here was 0.473 $M_\odot$, corresponding to an envelope mass of only 0.00162 $M_\odot$.

The ZAHB models computed in this manner were then evolved through the HB phase using standard algorithms for convective overshooting and semiconvection. The last model from each HB sequence was then used as the starting model for the subsequent AGB evolution. Mass loss was included in the AGB sequences, using the Reimers (1975) formulation for three values of η_R: 0.0 (no mass loss), 0.4, and 1.0. Note that these assumptions for AGB mass loss have no consequence for the AGB-Manqué evolution, because such stars do not ascend

the AGB (see §1). For this reason, and because we lack color information for these stars (given the one bandpass of our observations), we will only explore the models that assume $\eta_R = 0.4$ in our discussion below. The variation in mass loss may be explored in future work if color information becomes available for these stars.

The set of tracks with $\eta_R = 0.4$ consisted of 35 ZAHB masses (M_{ZAHB}), ranging from 0.473 to 0.700 $M_\odot$ and covering a temperature range from $log T_{\rm eff} = 4.42 - 3.67$. Due to mass loss on the AGB, the final masses on the white dwarf cooling curve (M_{WD}) for these tracks is somewhat less. AGB-Manqué behavior was found for stars with $M_{ZAHB} \leq 0.505\ M_\odot$; post-early AGB behavior for stars with $0.505 < M_{ZAHB} < 0.610\ M_\odot$ ($0.505 < M_{WD} < 0.542\ M_\odot$), and post-AGB behavior for stars with $M_{ZAHB} \geq 0.610\ M_\odot$ ($M_{WD} \geq 0.542\ M_\odot$).

These tracks permit the transition between the different classes of post-HB evolution to be much better defined than previously possible. Figure 7 shows examples of these evolutionary tracks as they appear in the STIS bandpass (see also Figure 1).

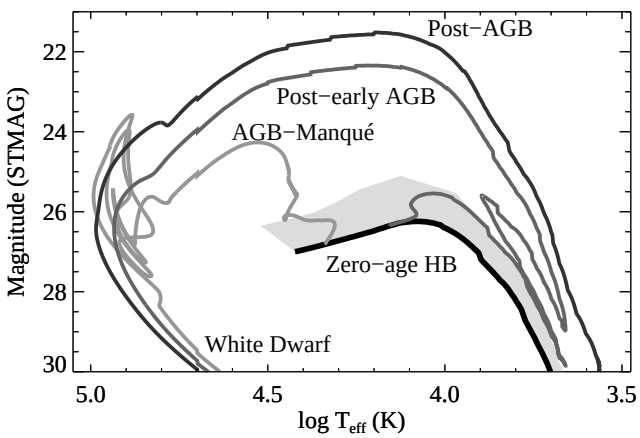

FIG. 7– The same tracks shown in Figure 1, but with luminosity replaced by magnitude in the STIS bandpass, under the STMAG system, assuming a distance of 770 kpc and $E(B-V) = 0.11$ mag. Note that assuming a lower reddening of $E(B-V) = 0.08$ mag would make the tracks ~ 0.25 mag brighter. The HB phase (again shown by light grey shading, as determined from our entire set of tracks), spans a range of 25–27 mag at $T_{\rm eff} > 8500$ K.

6.3.2. *Hot HB Luminosity Functions*

We have constructed the luminosity functions for each of the above HB and post-HB tracks in the STIS bandpass for comparison with the corrected STIS luminosity function given in Table 7. Because we only have one bandpass and no color information, it is difficult to constrain the mass distribution of stars on the hot HB. This difficulty is further compounded by the fact that post-AGB stars certainly contribute some small but non-negligible component to the STIS luminosity function, because we know the majority of the evolved population passes through some sort of post-AGB phase, given the weak UV upturn in M32. Color information would also help to separate these post-AGB stars from the rest of the STIS data, because they spend most of their time at much higher effective temperature.

The luminosity functions for four of our tracks can be added to create a composite luminosity function that agrees quite well with the STIS data (Figure 5). Two of these tracks follow AGB-Manqué evolution and two follow post-early AGB evolution upon leaving the HB. These tracks have been normalized to maximize agreement with the STIS data from 23–27 mag, and we show in Table 8 the relative contributions of these tracks to this composite LF. We stress that this LF serves as an example, to show that hot HB stars can reproduce the STIS luminosity function; color information is required to properly constrain the true distribution of mass on the hot HB. The STIS data confirm that stars passing through the hot HB at $T_{\rm eff} > 8500$ K comprise only a small fraction (approximately 7%) of the total HB population in M32. This fraction of hot HB stars would be somewhat lower if the contribution of the post-AGB stars could be subtracted from the STIS luminosity function.

Given the small fraction of the population entering the hot HB, we must conclude that the vast majority of the population passes through the red HB phase and the subsequent post-AGB evolution. Although a small population of hot HB stars can explain the numerous faint stars present in the STIS image, we still must explain the lack of bright stars. The likely explanation, as discussed in §6.2, is that the transition time from the AGB to the hotter post-AGB phases must be more rapid than that expected from the canonical low-mass H-burning tracks. The contribution of post-AGB stars to the STIS luminosity function would then be small, even though most of the population channels through post-AGB tracks.

TABLE 8: Hot HB Components of Composite LF

M_{ZAHB} ($M_\odot$)	ZAHB $T_{\rm eff}$ (K)	SEF (stars yr^{-1})	Fraction of total SEF
0.475	24578	1.95×10^{-5}	0.023
0.500	16372	3.03×10^{-6}	0.004
0.520	12034	6.20×10^{-6}	0.007
0.545	6057	3.20×10^{-5}	0.037

7. DISCUSSION

7.1. *Dynamical Creation Mechanism for Hot HB Stars?*

In the Galactic field, hot HB and post-HB stars are often found in binaries, and it has been suggested that a dynamical mechanism may play a role in the production of hot HB stars in old, metal-rich populations such as elliptical galaxies (Green et al. 1997; Green & Chaboyer 1998). In globular clusters, the role of dynamics remains a matter of debate. Horizontal branch morphology tends to become redder as metallicity increases, but examples of metal-rich GCs with blue HB morphology demonstrate that other parameters are at work (e.g., Rich et al. 1997). One of these parameters may be a dynamical mechanism, through binary or tidal interaction while on the RGB. There is some evidence that dynamics plays a role in HB morphology; e.g., Fusi Pecci et al. (1993) and Buonanno et al. (1997) demonstrated that more concentrated clusters have bluer HB morphologies with extended blue tails. Rich et al. (1997) found two metal-rich GCs with extended HB morphology (NGC6388 and NGC6441), although the evidence for a dynamical origin in that work appears inconclusive. These clusters have some of the highest values of central surface brightness, velocity dispersion, and stellar collision rates for Galactic GCs, which may partially explain their blue HBs, but Rich et al. (1997) find no evidence for a difference in the radial distribution of blue and red HB stars, as expected if tidal or binary interaction plays a role. Later work by Layden et al. (1999) did find that the blue HB stars in NGC6441 were more centrally concentrated than the red HB stars, but the difference in these gradients does not conform with theoretical expectations for a dynamical

mechanism, because it occurs too far from the cluster center. In NGC6752, Landsman et al. (1996) found that the hot HB is a continuous extension of the intermediate-temperature HB population, suggesting that a common single-star mechanism is responsible for both. In ω Cen, which has the largest known fraction of hot HB stars, D'Cruz et al. (1999) find no evidence for a radial gradient in the hot HB to red HB number ratio.

M32 is much smaller than other well-studied true ellipticals, and it has the lowest Mg_2 optical metallicity index of all the quiescent UV upturn galaxies in the Burstein et al. (1988) sample; in this sense, it is the elliptical galaxy that lies closest to the realm of globular clusters. However, elliptical galaxies should not be considered as overgrown globular clusters – they clearly inhabit a different regime of parameter space, especially when considering the evolved population of stars that produces the UV upturn. This is apparent in the modified version of the Burstein et al. (1988) $1550-V$ vs. Mg_2 relation shown by Dorman et al. (1995), which shows the GCs lying in a completely distinct clump removed from the tight E galaxy sequence. It is thus worth noting that the existence of hot HB stars in M32 cannot be easily explained by dynamical mechanisms, because the stellar densities in elliptical galaxies are so much lower than those in globular clusters (except for the very center of ellipticals, which often harbor a black hole). The central luminosity densities of NGC6388 and NGC6441 are respectively $1.86\times10^5\,L_\odot$ pc^{-3} and $2.00\times10^5\,L_\odot$ pc^{-3} (Djorgovski 1993). M32 has a luminosity density of $4.9\times10^5\,L_\odot$ pc^{-3} at a radius of $0.1''$, but this density drops rapidly by more than three orders of magnitude at radii greater than $8''$ (Tonry 1988; Gebhardt et al. 1996; private communication Gebhardt 1999). Furthermore, the far-UV to *B*-band flux ratio increases with radius in M32 (Ohl et al. 1998). Because our STIS data firmly demonstrate that the weak far-UV flux is due to hot HB stars, the increase in the far-UV to *B*-band flux ratio indicates that hot HB stars comprise a larger fraction of the population at increasing distance from the galactic center – again, opposite to the behavior expected from a dynamical creation mechanism such as tidal interaction or binarism.

7.2. *The Age of M32*

In recent years, much of the effort on dating M32 has shown a need for an intermediate-age ($\sim$ 5 Gyr) component to its population. When this fact is considered in tandem with its small size and proximity to M31, its utility as a template for other ellipticals is somewhat diminished. However, even though it may be unusual, M32 represents the only elliptical near enough for intense study by all of the standard stellar population analysis methods (spectroscopy, line indices, color-magnitude diagrams, etc.), at least until we have a successor to HST with UV-optical capability. With this in mind, are we certain that M32 has a younger component to its older, dominant population? We feel that this remains an open question.

Early color-magnitude diagrams reported evidence for a younger population by finding very bright AGB stars, but later interpretations of these data showed that both crowding (Renzini 1998) and long-period variables (Guarnieri et al. 1997) confused the earlier analysis; later observations (Grillmair et al. 1996) also find no evidence for optically bright AGB stars, but these stars were difficult to detect in the *V* band. Instead, it appears that the brightest AGB stars in M32 are consistent with those found in other old globular clusters (Guarnieri et al. 1997; Renzini 1998). We note that our own data show a lack of the very bright post-AGB stars that should be present if they are leaving the tip of the AGB at luminosities much brighter than the RGB tip.

Spectral synthesis analyses using isochrones like those of Worthey (1994) assume a pure red clump HB morphology, and the STIS data show that this assumption is not entirely accurate; note, however, that the Worthey models were not intended to address UV flux. Depending upon how much of the population extends beyond the red clump, an analysis that assumes a pure red clump may be seriously incorrect. Our data demonstrate that the hot horizontal branch is populated in M32, but the lack of color information prevents us from constraining the HB morphology further. The tracks that reproduce the STIS luminosity function come from a wide range of $T_{\rm eff}$ on the HB (see Table 8), and so they are consistent with both a bimodal HB distribution and with an extended, more uniform distribution. However, the integrated spectrum of M32 does not show the strong 2500 Å dip seen in UV-bright quiescent giant ellipticals (compare Figure 4 with the spectra of Burstein et al. 1988 and Brown et al. 1997). Given the presence of hot HB stars and the missing 2500 Å dip, the distribution of effective temperature on the HB might be more uniform in M32 than the strongly bimodal distributions assumed in giant ellipticals. The zero-age HB becomes more bimodal at increasing metallicity and helium abundance (see Dorman et al. 1993); because M32 has an abundance much closer to solar than the giant ellipticals (see Burstein et al. 1988), evolution theory favors a more uniform HB. Our hot HB model population (Table 8), if correct, would be responsible for practically all of the flux at 2500 Å, and contribute to approximately 10% of the flux from 3000–4000 Å, even though it only comprises a small fraction of the HB population ($\sim$5%). Thus, this hot HB component should not be ignored for population fitting in the mid-UV.

The H_β (λ 4861 Å) line index is often quoted as another piece of evidence in favor of a young component in M32. It is significantly stronger in M32 than in the higher metallicity giant ellipticals (Bressan, Chiosi, & Tantalo 1996; Burstein et al. 1984), with an equivalent width (EW) of 2.2 Å compared to an average value of 1.7 Å. Metal-poor globular clusters have even stronger H_β absorption than M32 (as high as 3 Å EW), but the index decreases in strength at increasing metallicity, and high metallicity globular clusters show a weaker index than in M32 (Burstein et al. 1984). Note, however, that these earlier studies did not include metal-rich GCs with blue HB morphology, such as those studied by Rich et al. (1997). Burstein et al. (1984) claim that the addition of early A stars to the old stellar population in M32 can increase the H_β appropriately, but the resulting UV continuum would be too bright, and instead favor later main-sequence F stars. Note that there is a radial gradient to the H_β absorption in M32, in the sense that it is significantly weaker in the deepest parts of the STIS image, compared to the galactic center (González 1993; Hardy et al. 1994); this suggests that the younger population, if present, is most prevalant in the nucleus (see Grillmair et al. 1996).

It is possible instead that intermediate-temperature HB stars could account for *some* of the extra H_β absorption (assuming that M32 has a less bimodal HB mass distribution than seen in giant ellipticals), but it is unlikely, given our data and models, that the HB could account for *all* of this extra absorption. Approximately 20% of the light at H_β comes from the horizontal branch (see, e.g., Yi, Demarque, & Oemler 1997). Thus, if a large fraction of the ZAHB population was at F-star temperatures (near 7000 K), the H_β absorption would increase signifi-

cantly. Specifically, a small set of synthetic spectra calculated for this purpose, using SYNSPEC (Hubeny, Lanz, & Jeffery 1994) and Kurucz (1993) model atmospheres, shows that the H_β EW increases from 1.2 Å at T_{eff} = 5000 K to 8 Å at 7500 K (measuring EW as in Faber et al. 1985), eventually peaking to 9.5 Å at 9000 K. ZAHB stars near 7000 K would lie at the very faint (and incomplete) end of the STIS luminosity function (see Figure 7), and thus could be present in large numbers. However, these stars become post-early AGB stars in their later and brighter phases, and if such tracks are populated at significant levels ($\sim$ 50%), the STIS luminosity function would have many more UV-bright stars than we actually see. Note that the hot-HB model population shown in Table 8 comprising $\sim$ 5% of the HB population, would only contribute to $\sim$ 5% of the flux at H_β. One could place a large fraction of the ZAHB near 7000 K (thus accounting for all of the H_β absorption) only if the later, UV-bright post-early-AGB phases were more rapid than predicted from the models, as seen for the post-AGB stars. Thus, even with a hot HB component in M32, the H_β absorption might be the one piece of evidence that is difficult to explain without some trace of younger stars or blue stragglers.

7.3. *Summary*

The STIS data presented here are the first to directly image stars on the hot horizontal branch in any elliptical galaxy. In previous work, the spectral energy distribution and the magnitude of the far-UV flux in giant ellipticals required the presence of hot HB stars, unless UV-bright post-AGB stars were much more efficient UV emitters than thought previously. Until these STIS observations, M32 was the one example of an elliptical where the weak UV flux could have been explained by canonical low-mass post-AGB tracks. Our data show that the hot HB is populated in M32, and that the UV-bright phases of post-AGB evolution are less populated than expected from canonical tracks; thus these data represent a direct confirmation that the UV upturn in ellipticals originates in hot HB stars. Our findings demonstrate that M32 does not have a pure "red clump" HB morphology, as assumed by many of the stellar population analyses of this galaxy. If the HB effective temperature distribution is not extremely bimodal, our findings may weaken the evidence for an intermediate age population in M32. Color information would best constrain the HB morphology further, and we will propose to carry out far-UV imaging of this same field in the coming HST cycle; the far-UV data would provide an excellent discriminator between stars hotter and cooler than 12000 K, which would constrain the bimodality of the HB in M32. Furthermore, color information will allow us to discern how many of the faint stars in our luminosity function are on the white dwarf cooling curve, and this may shed light on the evolution of post-AGB stars, which appear to be evolving rapidly in the STIS field.

Support for this work was provided by NASA through the STIS GTO team funding. TMB acknowledges support at Goddard Space Flight Center by NAS 5-6499D. We wish to thank K. Gebhardt for kindly providing the luminosity density profile of M32. We also wish to thank P. Stetson, who provided the DAOPHOT-II package and gave us assistance with its use. This research has made use of the SIMBAD database, operated at CDS, Strasbourg, France.

REFERENCES

Baum, S., et al. 1998, Space Telescope Imaging Spectrograph Instrument Handbook, (Baltimore: STScI), 315
Bertelli, G., Bressan, A., Chiosi, C., Fagotto, F., & Nasi, E. 1994, A&AS, 106, 275
Bertola, F.,Bressan, A., Burstein, D., Buson, L. M., Chiosi, C., & Alighieri, S. D. S. 1995, ApJ, 438, 680
Bressan, A., Chiosi, C., & Tantalo, R. 1996, A&A, 311, 425
Brown, T.M., Ferguson, H.C., Davidsen, A.F., & Dorman, B. 1997, ApJ, 482, 685
Brown, T. M., Ferguson, H. C., Stanford, S. A., & Deharveng, J.-M. 1998, ApJ, 504, 113
Buonanno, R., Corsi, C., Bellazzini, M., Ferraro, F. R., & Fusi Pecci, F. 1997, AJ, 113, 706
Burstein, D., Bertola, F., Buson, L. M., Faber, S. M., & Lauer, T. R. 1988, ApJ, 328, 440
Burstein, D., Faber, S. M., Gaskell, C. M., & Krumm, N. 1984, ApJ, 287, 586
Burstein, D., & Heiles, C. 1984, ApJS, 54, 33
Cardelli, J. A., Clayton, G. C., & Mathis, J. S. 1989, 345, 245
Ciardullo, R., Jacoby, G. H., Ford, H. C., & Neill, J.D. 1989, ApJ, 339, 53
Code, A.D. 1969, PASP, 81, 475
Da Costa, G.S. 1997, in Proc. Eigth Canary Islands Winter School, Stellar Astrophysics for the Local Group, ed. A. Aparicio & A. Herrero (Cambridge: Cambridge Univ. Press), 351.
D'Cruz, N. L., O'Connell, R. W., Rood, R. T., Whitney, J. H., Dorman, B., Landsman, W. B., Hill, R. S., Stecher, T. P., & Bohlin, R. C. 1999, ApJ, submitted
Djorgovski, S. 1993, in ASP Conf. Proc. 50, Structure and Dynamics of Globular Clusters, ed. S. G. Djorgovski & G. Meylan (San Francisco: ASP), 373
Dopita, M. A., Jacoby, G. H., & Vassiliadis, E. 1992, ApJ, 389, 27
Dorman, B., O'Connell, R.W., & Rood, R.T. 1995, ApJ, 442, 105
Dorman, B., Rood, R.T., & O'Connell, R.W. 1993, ApJ, 419, 596
Faber, S. M., Friel, E., Burstein, D., & Gaskell, C. M. 1985, ApJS, 57, 711
Ferguson, H. C., & Davidsen, A. F. 1993, ApJ, 408, 92
Fusi Pecci, F., & Bellazzini, M. 1997, in Third Conference on Faint Blue Stars, ed. A. G. Davis Philip, J. W. Liebert, & R. A. Saffer (Schenectady: L. Davis Press), 255
Fusi Pecci, F., Ferraro, F. R., Bellazzini, M., Djorgovski, S., Piotto, G., & Buonanno, R. 1993, AJ, 105, 1145
Gardner, J. P., et al. 1999, AJ, submitted
Gebhardt, K., Richstone, D., Ajhar, E. A., Lauer, T. R., Byun, Y.-I., Kormendy, J., Dressler, A., Faber, S. M., Grillmair, C., & Tremaine, S. 1996, AJ, 112, 105
González, J. 1993, Ph.D. thesis, University of California, Santa Cruz
Green, E. M., & Chaboyer, B. C. 1998, BAAS, 30, 1404
Green, E. M., Liebert, J. W., Peterson, R. C., & Saffer, R. A. 1997, in Third Conference on Faint Blue Stars, ed. A. G. Davis Philip, J. W. Liebert, & R. A. Saffer (Schenectady: L. Davis Press), 271
Greenfield, P. 1994, in Instrument Science Report FOC-075, Format-Dependent Sensitivity Effects, http://www.stsci.edu/ftp/instrument_news/FOC/Foc_isr/foc_isr075.ps
Greggio, L., & Renzini, A. 1990, ApJ, 364, 35
Greggio, L., & Renzini, A. 1999, in UV Astronomy in Italy, ed. L. M. Buson & Domitilla De Martino, in press.
Grillmair, C. J., et al. 1996, AJ, 112, 1975
Guarnieri, M. D., Renzini, A., & Ortolani, S. 1997, ApJ, 477, L21
Hardy, E., Couture, J., Couture, C., & Joncas, G. 1994, AJ, 107, 195
Hubeny, I., Lanz, T., & Jeffery, C. S. 1994, in Newsletter on Analysis of Astronomical Spectra No. 20, ed. C. S. Jeffery (CCP7; St. Andrews: St. Andrews Univ.), 30
Käufl, H. U., Renzini, A., & Stanghellini, L. 1993, ApJ, 410, 251
Kimble, R. A., et al. 1998, ApJ, 492, 83
King, I. R., et al. 1992, ApJ, 397, L35
Kurucz, R. L. 1993, CD-ROM 13, ATLAS9 Stellar Atmosphere Programs and 2 km/s Grid (Cambridge: Smithsonian Astrophys. Obs.)
Landsman, W. B., Sweigart, A. V., Bohlin, R. C., Neff, S. G., O'Connell, R. W., Roberts, M. S., Smith, A. M., & Stecher, T. P. 1996, ApJ, 472, L93
Layden, A. C., Ritter, L. A., Welch, D. L., & Webb, T. M. A. 1999, AJ, 117, 1313
McClure, R. D., & Racine, R. 1969, AJ, 74, 1000
O'Connell, R. W. 1999, in Annual Reviews of Astronomy & Astrophysics, in press
Ohl, R. G., O'Connell, R. W., Bohlin, R. C., Collins, N. R., Dorman, B., Fanelli, M. N., Neff, S. G., Roberts, M. S., Smith, A. M., & Stecher, T. P. 1998, ApJ, 505, L110
Reimers, D. 1975, Mém. Roy. Soc. Liège, 8, 369
Renzini, A. 1989, in Planetary Nebulae, ed. S. Torres-Peimbert (Dordrecht: Kluwer), 391
Renzini, A. 1998, AJ, 115, 2459
Renzini, A., & Fusi Pecci, F. 1988, ARA&A, 26, 199

Rich, R. M., et al. 1997, ApJ, 484, L25
Schönberner, D. 1987, in IAU Symposium 131, Planetary Nebulae, ed. S. Torres-Peimbert (Dordrecht: Kluwer Academic Publishers), 463
Stetson, P. B. 1987, PASP, 99, 191
Sweigart, A. V. 1999, in Spectrophotometric Dating of Stars and Galaxies, ed. I. Hubeny, S. Heap, & R. Cornett, (San Francisco: ASP), in press
Tonry, J. L. 1988, in Dynamics of Dense Stellar Systems, ed. D. Merritt, (Cambridge: Cambridge University Press), 35
Tully, R. B. 1988, Nearby Galaxies Catalogue (Cambridge: University Press)
VandenBerg, D. A., 1999, in The Third Stromlo Symposium: The Galactic Halo, ed. B. K. Gibson, T. S. Axelrod, & M. E. Putman (San Francisco: ASP), 46
Vassiliadis, E., & Wood, P. R. 1993, ApJ, 413, 641
Vassiliadis, E., & Wood, P. R. 1994, ApJS, 92, 125
Woodgate, B. E., et al. 1998, PASP, 110, 1183
Worthey, G. 1994, ApJS, 95, 107
Yi, S., Demarque, P., & Oemler, A., Jr. 1997, ApJ, 486, 201